

Spectral shadows of a single GaAs quantum dot

Kai Hühn,^{1,2} Lena Klar,^{1,2} Fei Ding,^{1,2} Arne Ludwig,³ Andreas
D. Wieck,³ Jens Hübner,^{1,2,*} and Michael Oestreich^{1,2,†}

¹*Institut für Festkörperphysik, Leibniz Universität Hannover, Appelstraße 2, 30167 Hannover, Germany*

²*Laboratory of Nano and Quantum Engineering,*

Leibniz Universität Hannover, Schneiderberg 39, 30167 Hannover, Germany

³*Lehrstuhl für Angewandte Festkörperphysik, Ruhr-Universität Bochum, DE-44780 Bochum, Germany*

(Dated: July 29, 2025)

Semiconductor quantum dots are a promising platform for generating single and entangled photons. Still, their use is limited even in the most advanced structures by changes in the charge state of the quantum dot and its environment. Here, we present detailed time-resolved resonance fluorescence measurements on a single charge-tunable GaAs quantum dot, shedding new light on the spectral shadows invoked by the complex impurity environment. Detuning-dependent measurements reveal the existence of multiple Stark-shifted resonances, which are associated with rare spectral jumps smaller than the homogeneous linewidth and, therefore, typically concealed in the measurement noise. We observe similar environmentally induced Stark shifts for both the neutral exciton and negatively charged trion transitions, while the positively and doubly negatively charged trions exhibit significant differences. Our investigation quantifies the underlying impurity charge dynamics over a range from well below milliseconds to seconds, revealing that the hole occupation of the positively charged trion transition is constrained by rapid hole loss and slow hole recapture dynamics. Utilizing a second non-resonant laser, we increase the hole occupancy by over an order of magnitude and identify both a prolonged hole residence time and an enhanced hole tunneling rate into the quantum dot. These findings are supported by complementary spin noise spectroscopy measurements, which offer a significantly higher bandwidth compared to the time-resolved resonance fluorescence measurements.

I. INTRODUCTION

Semiconductor quantum dots (QDs) provide a promising platform for single and entangled photon sources, quantum repeaters, spin and photon-based quantum logic, and quantum light sources for quantum imaging [1–3]. Compared to single atoms, individual QDs offer significantly greater flexibility in terms of experimental accessibility and engineering of their optical properties. However, despite the tremendous progress in the growth and manufacturing processes of such QDs, there are still several obstacles that limit their optimal use in quantum devices. One major obstacle are impurities in the surrounding solid-state matrix that lead to charge noise and result in stochastic shifts of the Fourier transform-limited QD transitions, blinking, and decoherence. This noise can be strongly reduced by embedding the heterostructure containing the QD layer in a PIN diode structure. However, some noise remains even in the most advanced PIN structures. This noise reveals itself in time-dependent spectral shadow resonances, which will be centrally addressed in this work, and is accompanied by charge-changing Auger recombination in the case of resonant excitation of charged exciton resonances.

The influence of charge and spin fluctuations on QD transitions has been a focus of extensive research by various groups in recent years. Notably, Warburton et al. demonstrated through several seminal studies that single-charge fluctuations at the GaAs/(AlGa)As interface of a Schottky diode yield significant step-like Stark shifts of a nearby (InGa)As QD resonance. They concluded from a comparison of their experimental results with a straight-forward theoretical model that

the relevant charge centers are localized holes at the GaAs/(AlGa)As interface and that these charge centers are not just randomly distributed in the 2D plane. Instead, the QD itself induces the formation of a small number of localization centers directly above the QD due to strain from the (InGa)As lattice mismatch and the roughness of the closely adjacent GaAs/(AlGa)As interface [4]. They also studied the temporal dynamics of charge and spin noise of a single (InGa)As QD in an ultra-clean quantum device for frequencies from 0.1 Hz to 100 kHz and showed that charge noise dominates especially at low frequencies, and demonstrated transform-limited QD optical linewidths by operating the device above 50 kHz [5]. Subsequently, Hauck et al. used resonant laser spectroscopy of multiple (InGa)As QDs to spatially locate charge fluctuators in the surrounding semiconductor matrix of a QD [6]. They suggested that not only holes at a hetero-interface but also residual carbon dopants in the bulk can act as major charge-fluctuating traps in QD heterostructures. They explained the observed steady-state observation of the impurity sites by hole tunneling between the carbon impurity and 2D hole gas resonances. Around the same time, Matthiesen et al. realized stabilization of the charge environment of a single QD by implementing a feedback loop using the phonon-assisted component of the resonance fluorescence to stabilize the frequency and photon emission rate of the zero-phonon transition [7]. Shortly after, Ha et al. reported on the spectral diffusion of GaAs QDs as a result of fluctuating surface charges with dependence on morphology [8]. More recently, the group of Geller et al. demonstrated photon noise suppression by a built-in feedback loop [9] and the use of single QDs as a quantum sensor to characterize the position and activation energy of individual shallow impurities on the nanoscale [10] while Zhai et al. realized an optimized PIN diode with low-noise GaAs QDs [1].

* jhuebner@nano.uni-hannover.de

† oest@nano.uni-hannover.de

Most of these experiments rely on resonance fluorescence (RF) spectroscopy in PIN diode structures. Tuning the RF laser to specific QD resonances allows for selective probing of particular charge states and the real-time observation of charge dynamics, including carrier capture, tunneling events, or relaxation processes. Experiments using pulsed RF measurements on (InGa)As QDs, coupled to a charge reservoir through a 30 nm tunnel barrier, revealed for example electron tunneling rates in the QD γ_e of 200 kHz and Auger emission rates γ_a of 500 kHz [11]. These Auger emission rates are of interest because the homogeneous QD linewidth is broadened and the photon emission rate is quenched for high ratios of γ_a/γ_e . Auger rates in (InGa)As QDs have also been investigated using spin noise spectroscopy (SNS), reporting hole emission rates of 2 MHz, which limits the hole spin lifetime for resonant experiments [12]. Recent advancements in time-resolved RF measurements have enabled optical real-time monitoring of single-electron tunneling events. In conjunction with full counting statistics evaluation methods, a new benchmark was established in the study of Auger emissions. Measurements using this method revealed additional, unassigned electron spin relaxation channels with a common rate of 3 kHz for (InGa)As QDs [13]. Real-time RF measurements using two colors allowed further studies of Auger events in a single QD [14]. An Auger emission time of 1.7 μ s and electron tunnel rates of 1 kHz have been reported for a tunnel barrier with a thickness of 45 nm. As expected, the effective Auger rate can be controlled by the probe beam power and shows a linear dependence. Other two color experiments using low-energy photons revealed the photoeffect as a previously unnoticed non-resonant charge-loss channel for QDs [15]. Shortly after, this photoeffect was confirmed in SNS experiments in single (InGa)As QDs [16].

II. EXPERIMENTAL DETAILS

In the following, we will study by time-resolved RF spectroscopy the carrier dynamics in and around a nearly unstrained single GaAs QD located in an optimized, low-noise PIN diode structure. We will quantitatively resolve charge-induced shifts of the QD resonance, which are significantly smaller than the homogeneous QD transition linewidth, discuss the charging dynamics and the impact of non-resonant optical excitation, and show how charging dynamics occurring faster than typical RF binning affect the RF spectrum.

The high quality GaAs QDs are grown by molecular beam epitaxy using the well-developed nanodroplet technology [17, 18]. The QDs are embedded in a PIN diode structure, which allows for a deterministic charging of the QD and strongly reduces the environmental charge noise. The pin structure consists of a 150 nm Si-doped ($\text{Al}_{0.15}\text{Ga}_{0.85}$)As n-contact, an undoped 20 nm ($\text{Al}_{0.15}\text{Ga}_{0.85}$)As and 10 nm ($\text{Al}_{0.33}\text{Ga}_{0.67}$)As tunneling barrier, 0.3 nm AlAs, droplet etched GaAs QDs, an undoped 274 nm ($\text{Al}_{0.33}\text{Ga}_{0.67}$)As and 75 nm ($\text{Al}_{0.15}\text{Ga}_{0.85}$)As spacer layer, and a 5 nm C-doped GaAs p-contact. Figure 1(a) depicts the corresponding band structure and Fig. 1(b) a spatially

and spectrally resolved photoluminescence (PL) map of the sample at a temperature of 4 K and zero bias voltage. We consistently present results from the same QD throughout this publication. The QD is marked in Fig. 1(b) by a blue circle and exhibits a single PL emission line at low excitation intensities (not displayed), which is spectrally well separated from the emission lines of the neighboring QDs that emit at higher energies.

The PL and RF measurements are performed in a high-resolution confocal microscope setup with a focal spot diameter of $\lesssim 1 \mu\text{m}$ in reflection geometry using tunable diode and Ti:Sapphire ring lasers. For PL measurements, the QDs are excited nonresonantly by a diode laser with a photon energy of 1.63 eV, and the detected PL of individual QDs is spectrally resolved using a triple-stage spectrometer with a maximal resolution of 20 μeV and a liquid-nitrogen-cooled CCD camera. For RF measurements, the excitation laser is suppressed using a cross-polarization extinction technique [19] without any additional wave plates, achieving a signal to background extinction ratio of about $1 : 10^{-6}$. In the two-color experiments, the nonresonant laser is further suppressed using a band-pass filter [20]. The photons emitted by the QD are detected by a single-photon avalanche photo diode (APD) [21], and a high-speed digitizer card [22] records the arrival times of single photons from the APD. The sample is kept continuously in a closed-cycle cryostat at a temperature of 4 K, allowing extended measurement durations without recurrent thermal cycling for coolant replacement. High-precision, low-temperature piezo actuators [23] provide accurate and stable position control.

III. QD CHARGE AND CHARGING DYNAMICS

A detailed characterization of the QD and its static charge state is carried out by RF in dependence on gate voltage (V_G) and RF probe laser energy. Figure 2 depicts the two-dimensional RF measurement revealing distinct charge plateaus for the positively charged trion (X^+), the neutral exciton (X), the negatively charged trion (X^-), and the double negatively charged exciton (X^{2-}) transition. The assignment of the transitions is confirmed by polarization and V_G dependent PL measurements which yield a fine structure splitting of the neutral exciton of 1.6(1) μeV and, as expected, no splitting for the negatively charged trion transition. In the following, we focus on the X^+ , X , X^- , and X^{2-} ground state transitions whereas the V_G dependent PL measurements even clearly identify the ground state transitions of the QD charged from fourfold positively (X^{4+}) to sixfold negatively (X^{6-}) (see Appendix A).

The QD transitions in Fig. 2 show a clear dependence on V_G due to the quantum confined Stark effect. In general, the exciton transition energy, E_X , exhibits a linear and quadratic dependence on the local electric field amplitude in z -direction, F_z , according to [24, 25]:

$$E_X(F) = E_X(0) - p_z F_z + \beta F_z^2, \quad (1)$$

where $E_X(0)$ is the exciton transition energy in the absence of an externally applied electric field, p_z is

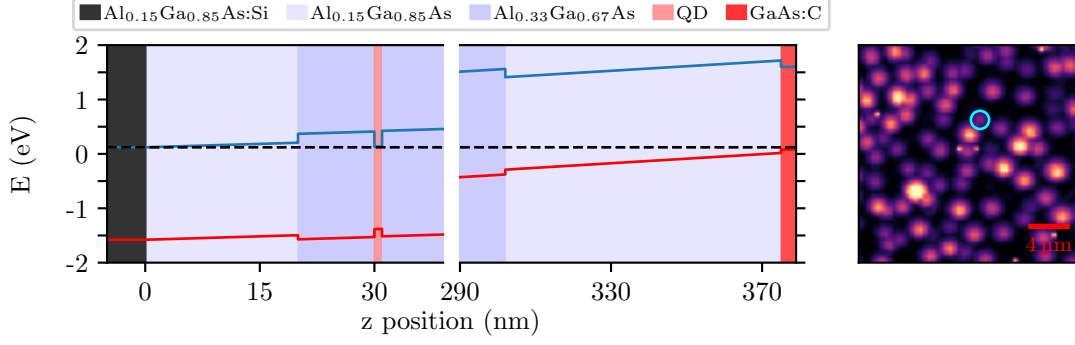


Figure 1. (Left) Schematic band structure of the sample including the QD layer located 30 nm from the n-contact and 349 nm from the p-contact. The black horizontal dashed line depicts the Fermi-level at zero bias. (Right) Photoluminescence map with the QD of interest marked by a blue circle.

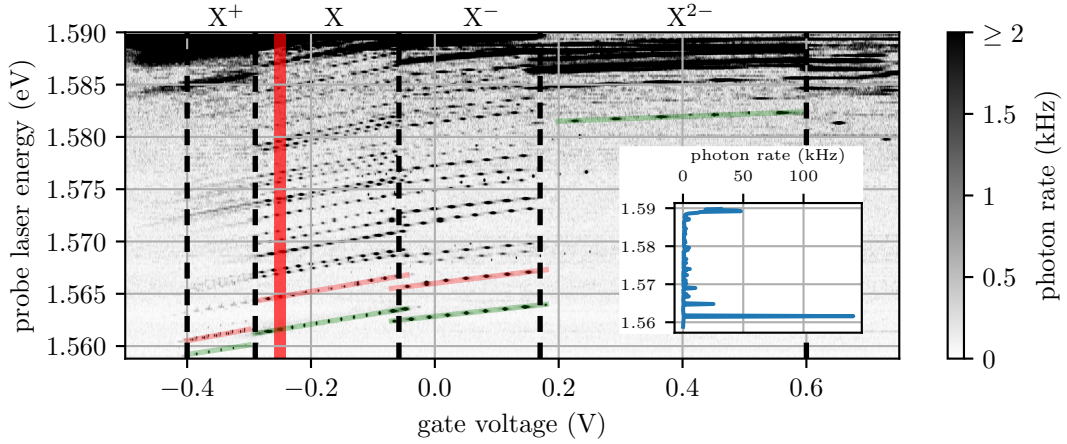


Figure 2. Resonance fluorescence measurements showing the charge plateaus from X^+ to X^{2-} , including both ground and numerous excited states. Ground states ($n=1$) are highlighted in green and the first excited states ($n=2$) in red. The greyscale colour code of the photon rates is adapted so that even low photon rates are visible. The resonance plateaus appear discontinuous due to the $200 \mu\text{eV}$ step size of the laser's photon energy employed in this experiment. The inset depicts exemplarily the average photon rate measured in the regime marked in red.

the accessible part of the permanent dipole moment arising from the intrinsic spatial separation of electron and hole in the unisotropic QD, and β the polarizability of the electron-hole pair. A fit to the measured exciton ground state transition energy versus V_G yields $p = 9.1(0) \text{ meV} \cdot (380 \text{ nm/V})$ and $\beta = -2.7(1) \text{ meV} \cdot (380 \text{ nm/V})^2$. For the trion states, the additional carrier in the QD partially screens the electric field. This screening is negligible in the case of X^+ since the holes are significantly stronger localized than the electrons. In fact, the measured dipole moment p_z is identical for X and X^+ within the error bars. In contrast, p_z decreases for X^- and X^{2-} significantly by 26 % and 54 %, respectively, while the respective β decreases by 13 % and increases by 57 %. For X^+ , β decreases by 63 %. We want to point out that these changes of β strongly depend on the QD morphology and charge occupation, making theoretical predictions difficult.

In the following, we will use the quantum confined Stark shift of the QD as a probe for the local electric field in order to measure the charging dynamics of the QD and its surroundings. Figure 3(a) shows a typical telegraph-like signal recorded on the X transition for a

detuning from the transition maximum of $0.29 \mu\text{eV}$. For these measurements, the single-photon events detected by the APD are grouped into non-overlapping time intervals with a binning period t_b (typically 1 ms). Most of the time, the RF photon rate in Fig. 3(a) remains steady at approximately 300 kHz, but it occasionally drops suddenly to about 13 kHz for a brief period. This drop results from a charge change of the QD surroundings, which shifts the QD resonance slightly. In contrast, a change of the charge state of the QD itself results in a significant jump in the transition energy, as can be seen from Fig. 2, which is much larger than the QD linewidth, resulting in a reduction of the RF to effectively zero. Figure 3(b) shows the same measurement as Fig. 3(a) but depicts the relative probability of each photon rate in blue. The black dashed line in Fig. 3(b) presents the respective shot noise level calculated for the high and low photon count rate and $t_b = 1 \text{ ms}$. The agreement of the measured data with the calculated shot noise level clearly shows that the measurement is shot noise limited. An increase of t_b reduces the relative shot noise level but degrades the time resolution and vice versa. The peak observed at a very low photon rate corresponds to a non-bright state. In this case, the

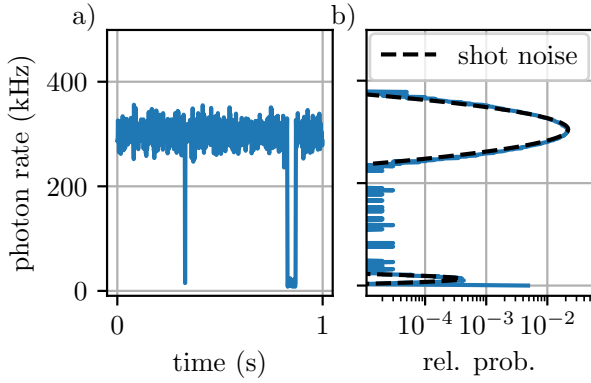


Figure 3. (a) Typical telegraph-like signal recorded on the neutral exciton transition for a detuning of $0.29 \mu\text{eV}$. Generally, the photon emission rate remains steady at approximately 300 kHz , but occasionally it abruptly decreases to lower rates. (b) Relative probabilities of the telegraph photon rates. The two distinct peaks superimposed by black dashed lines correspond to states with high and low RF photon rates. The third peak at 1 kHz corresponds to a non-bright state.

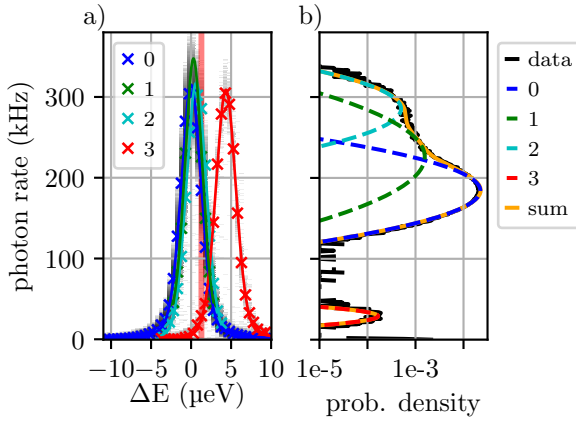


Figure 4. The measured detuning dependence of the photon rate (a) reveals in combination with the photon rate probability density (b) four clearly distinguishable states: the dominant resonance 0, two weakly shifted resonances 1 and 2, and the strongly shifted resonance 3. The relative occurrences of the states 0 to 3 evaluate to 90.9% , 6.3% , 2% , and 0.7% .

resonance is far detuned from the probing laser energy and the detected photons result solely from leakage due to limited polarization extinction and from the intrinsic APD background count rate of about 50 Hz . The area of each peak is proportional to the occurrence probability of the corresponding scenario (78.6% , 19.9% , and 1.5%) [26].

Next, we repeatedly conduct the experiment shown in Fig. 3, varying the detuning energy ΔE of the laser from the maximum of the dominant X resonance. This approach provides detailed insights into the relevant number of impurities in the QD surroundings and their charging dynamics. In fact, the approach reveals that not two charge configurations are relevant, as suggested by Fig. 3(b), but four. Figure 4(a) shows the measured RF photon rate, in a grayscale colour code, as a function

of ΔE . Additionally, Fig. 4(b) depicts exemplarily the probability density of the photon rate for a particular ΔE , which is marked by a red vertical line in Fig. 4(a). This probability density of Fig. 4(b) can be perfectly fitted by a sum of four, shot noise limited Gaussian curves. Each of these curves results from a specific charging configuration of the surrounding, labeled 0 to 3. The center positions of the four Gaussian curves specify the respective brightnesses of the four configurations at this particular ΔE and are marked in Figure 4(a) by crosses. Repeating this process and fitting the probability densities with an appropriate number of Gaussian curves for ΔE varying from $-10 \mu\text{eV}$ to $+10 \mu\text{eV}$, results in the crosses depicted in Figure 4(a). Further details concerning the telegraph data analysis are described in Appendix B. Finally, the crosses depicted in Figure 4(a) are fitted by four pseudo-Voigt functions, depicted by coloured lines, which yield the spectral position of the unshifted and shifted resonances. The analysis clearly shows four different charge configurations, denoted as RF QD shadows, three being very close in energy and one being shifted from the dominant state by about $4 \mu\text{eV}$. We emphasize that the likelihoods of the charge configurations 1 and 2 are by more than one order of magnitude lower compared to state 0 and that the respective energy shifts from the dominant state 0 are only $0.3 \mu\text{eV}$ and $0.6 \mu\text{eV}$, which are significantly smaller than the $3 \mu\text{eV}$ linewidth of the QD resonance. In fact, our analysis clearly distinguishes sparsely occupied shadow resonances, which are usually obscured by the dominant resonance in other experiments.

The occupation probability of the various impurity states and the screening of F_z are expected to depend on both the charge occupation of the QD and the chemical potential. Figure 5 compares the results from Fig. 4(a) for measurements on X with X^+ , X^- , and X^{2-} . In each case, the dominant resonance, marked in dark blue, occurs at the lowest energy. This corresponds to the highest electric field at the QD position. Since the relevant impurities are most likely Si impurities in the vicinity of the n-contact [27], this lowest energy corresponds to the scenario that all relevant Si impurities in the unintentionally doped (AlGa)As spacer between n-contact and QD being occupied by an electron. In principle, charge fluctuations from neighboring QDs could also influence the observed charging dynamics, but this scenario can be excluded with high probability based on an analysis of the shadow resonances as a function of gate voltage (data not shown). Neighboring QDs have, according to our PL measurements, a different ground state energy and therefore switch very likely at a different V_G ; however, the number and energy detuning of all observed shadow resonances of the investigated QD remain unchanged within the studied QD charge plateaus. Furthermore, optical excitation of neighboring QDs can be ruled out due to their spatial and spectral separation [28].

The quantum confined Stark shift, as detailed by Eq. 1 and quantified by Fig. 2, mainly varies between X and X^- . Taking this into consideration, Fig. 5 confirms that the configuration of active Si impurities is identical for both X and X^- . In contrast, no active Si impurities are observed for X^{2-} , suggesting that the

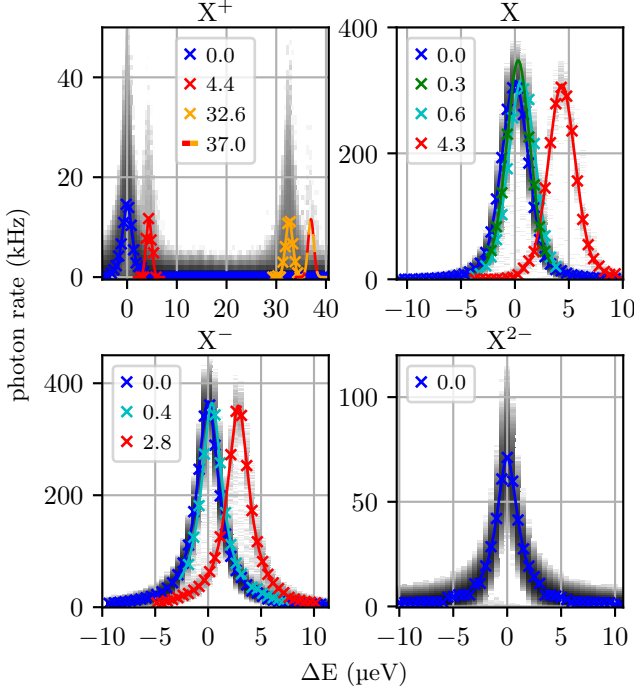


Figure 5. Probability densities as greyscale color code in dependence on ΔE for different QD charge states. The solid lines are fits to the observed resonances using pseudo-Voigt functions. The dominant transition is marked in dark blue and defines $\Delta E = 0$. The legend indicates the shift of the resonances in μeV .

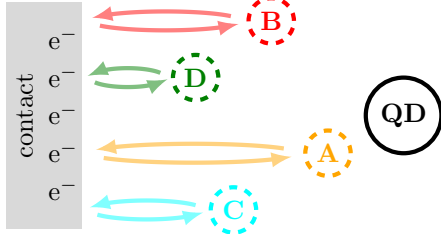


Figure 6. Schematic model of the active Si donor sites. Four distinct impurity sites are located at varying distances from the QD, each capable of trapping a single electron. Charge fluctuations of these sites induce local electric field changes, leading to characteristic shifts in the QD resonance energy.

electric field of the two QD electrons is strong enough to effectively suppress charge dynamics involving the surrounding Si impurities. For X^+ , on the other hand, Fig. 5 reveals a doublet structure, featuring a small shift of $4.4 \mu\text{eV}$ and a larger shift of about $30 \mu\text{eV}$. All four measured configurations in Fig. 5(a) to (d) are consistently explained by four distinct Si impurity sites, each situated at varying distances from the QD and capable of trapping a single electron. Figure 6 schematically illustrates the spatial configuration of these impurity sites, labeled from A to D, within the sample structure. Due to the Coulomb interaction between the QD and the impurity sites, not all impurity charge states manifest for a given charge in the QD. To describe the impurity charge states, the following notion is intro-

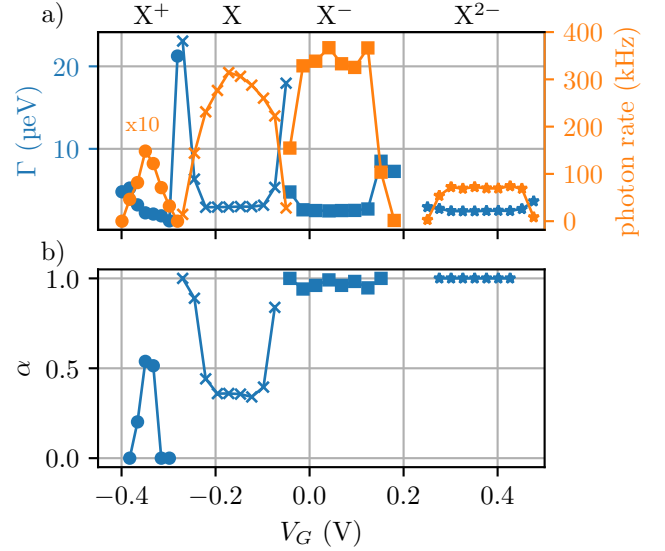


Figure 7. (a) Photon rates and linewidth Γ , and (b) fraction parameter α as a function of V_G for the dominant state 0, derived from pseudo-Voigt fits for X^+ to X^{2-} . The brightness of X^+ is multiplied by a factor of 10 for clarity. The solid lines serve as guides to the eye.

duced: $|A, B, C, D\rangle$, with $A, B, C, D \in \{-, e, 0\}$, where “-” indicates that the impurity charge state is constant over time, and e and 0 denote that the respective Si impurity can change its charge state and is currently charged (e) or not charged (0) with an electron. For X^+ , a doubled structure is observed with $|A, B, -, -\rangle$ where A is closest to the QD and therefore responsible for the large shift of $30 \mu\text{eV}$. The corresponding four impurity charge configurations are accordingly $|e, e, -, -\rangle$, $|e, 0, -, -\rangle$, $|0, e, -, -\rangle$, and $|0, 0, -, -\rangle$. For a charge of the QD corresponding to X and X^- , the Si impurity A becomes inactive, and the impurity configuration is described by $|-, B, C, D\rangle$. Three active states are responsible for the observed shifts, as any combination of only two does not produce the experimentally observed energy shifts. We want to point out that the experiment does not show all possible combinations of these states, suggesting that the impurities interact quite strongly with one another.

Next, we measure the influence of the fluctuating impurities on the dominant QD transition. Figure 7(a) depicts an analysis of photon rate and width of the dominant RF transition as a function of the gate voltage, providing insight into the stability and broadening mechanism of the different QD charge states. The photon rate of the X^+ state is by more than an order of magnitude lower compared to the X and X^- states and has a peak-like form, which indicates that the occupation of the QD by a hole is fragile. In fact, based on the band structure shown in Fig. 1(a), it is astonishing that this transition can be observed at all at this gate voltage and temperature, and the origin of a gate voltage induced hole in the QD is unclear. Unintentional carbon background doping and/or photo-induced carriers might play some role, but these assumptions could neither be confirmed nor rejected. Further studies concerning the X^+ transition by two-color, non-resonant

optical excitation are presented later in more detail. For X and X^- , the maximal RF photon rates are about equal at their respective charge plateaus, and the slightly higher maximal photon rate of X^- probably results mainly from its slightly narrower linewidth. Additionally, the photon rate of X also features a peak-like form, indicating the neutral charge state as more fragile compared to the negatively charged states. The photon rate of X^{2-} is by a factor of about six lower compared to X^- , which reflects the significantly lower oscillator strength of the $n = 2$ bound exciton state. The widths of X^{2-} and X^- are about equal since they are both dominated by the radiative lifetime of the excitonic $n = 1$ transition, i.e., the hole from the optically excited X^{2-} transition relaxes rapidly from $n = 2$ to $n = 1$. In the transition regimes from one charge state to another, the respective linewidth increases, and the photon rate drops drastically due to fast switching between two states. The sum of the two respective photon rates does not equal the average of the respective count rates at their peaks, since the fast switching leads to a strong broadening and reduction of amplitude of the respective transitions, and thereby to a reduced RF photon rate at a specific probing energy.

Figure 7(b) depicts the fraction parameter α from the pseudo-Voigt fit of the dominant transition in dependence on V_G . The parameter α determines the proportion of Gaussian and Lorentzian contributions, with $\alpha = 0$ indicating a purely Gaussian lineshape and $\alpha = 1$ indicating a purely Lorentzian lineshape. Interestingly, X^- and X^{2-} show in good approximation a purely Lorentzian profile, whereas X exhibits a mixture of Gaussian and Lorentzian. This suggests that, in this kind of low-noise PIN structure, both X^- and X^{2-} have the potential to outperform X in terms of achieving transform-limited single-photon emission. The lineshape of X becomes more Lorentzian and Γ larger in the transition regions from X towards X^+ and X^- , which is consistent with faster switching times, but this regime is less interesting for single photon sources.

Due to the PIN diode structure, electrons tunnel rather efficiently between n-contact and QD, and the number of electrons in the QD is easily adjusted by V_G . The tunneling of holes out of the QD can also be adjusted by V_G , but tunneling of holes into the QD is much slower and beyond the schematic band structure depicted in Fig. 1(a). Therefore, in order to study X^+ in greater detail, we employ an additional, weak, non-resonant laser excitation (NRE) with a photon energy of 1.61 eV. This energy is below the bandgap of the (AlGa)As barriers and excites non-resonantly additional electrons and holes directly in the QD. At V_G corresponding to X^+ , lost holes are thus efficiently replenished, while excess electrons and holes rapidly tunnel out of the QD, making X^+ in time average the most probable state.

Figure 8(a) depicts the resulting RF photon rate of the X^+ transition in dependence on the NRE power P^{NRE} for $\Delta E = -0.7 \mu\text{eV}$. As expected, the X^+ photon rate increases drastically with P^{NRE} , showing a typical saturation behaviour at high values. The solid orange

line represents a fit using the saturation model

$$\gamma_0^{ph}(P^{\text{NRE}}) = \frac{\gamma_0^{ph,max} \cdot P^{\text{NRE}}}{P_{sat}^{\text{NRE}} + P^{\text{NRE}}} + \gamma_0^{ph}(0), \quad (2)$$

with a peak photon rate $\gamma_0^{ph,max} = 159 \text{ kHz}$, a saturation power $P_{sat}^{\text{NRE}} = 81 \text{ nW}$, and a photon rate at zero NRE of $\gamma_0^{ph}(0) = 9.9 \text{ kHz}$, where the subscript 0 indicates the dominant state 0. For $P^{\text{NRE}} = 222 \text{ nW}$, Fig. 8(b) depicts the resulting detuning dependence for X^+ , which shows, next to an order of magnitude higher photon rate, two significant differences in comparison to no NRE. First, the NRE activates an additional, weak shadow resonance, and second, the Gaussian peaks only describe the most probable photon count rates at a given ΔE , whereby a significant background arises at lower photon rates. The change of the photon rate probability distribution with NRE is depicted more clearly in Fig. 8(c) for $\Delta E = -0.7 \mu\text{eV}$. The blue dots show the experimental results and the red line a simulation of the telegraph signal. The simulation includes the dominant state, a dark state, and a rapid, NRE induced switching of 2 ms (see Appendix B for details on the simulation). The shadow resonances observed in Fig. 8(b) are disregarded in the simulation due to their relatively low magnitude compared to the background. The straightforward simulations clearly suggest that the background arises from fast, NRE induced switching events of the transition. This is confirmed by spin noise spectroscopy (SNS) measurements, which have been carried out on the identical X^+ transition (see Appendix C for details on the SNS measurements). The SNS measurements also reveal that not only does the hole recharging of the QD speed up with increasing NRE power, as shown by RF in Fig. 8, but also that the tunneling rate out of the QD decreases with increasing NRE power.

IV. CONCLUSION

This study examined a single GaAs QD in terms of its impurity environment, identifying several adjacent impurity sites that cause spectral shifts of the QD transition. The time-resolved, single-photon resonance fluorescence measurements not only show the typical jumps of tenths of μeV of the QD transitions but also identify shifts which are significantly smaller than the QD's homogeneous linewidth and occur rarely. These small shifts are not resolved in standard RF measurements but influence the fidelity of single-photon sources based on QDs. The measurements suggest that the shifts result from charge fluctuations of Si donors, which are close to the Si-doped n-contact. Avoiding these Si donors is challenging since the diffusion constant of Si in (AlGa)As is significantly larger than for C [29, 30]. An effective solution might involve slightly increasing the Al fraction at the interface transition from Si-doped to undoped (AlGa)As. This adjustment would elevate the energy levels of the detrimental Si impurities, reducing the probability of charge fluctuations. However, care must be taken not to incorporate DX centers with energy levels below the conduction band by increasing the Al-concentration [31, 32].

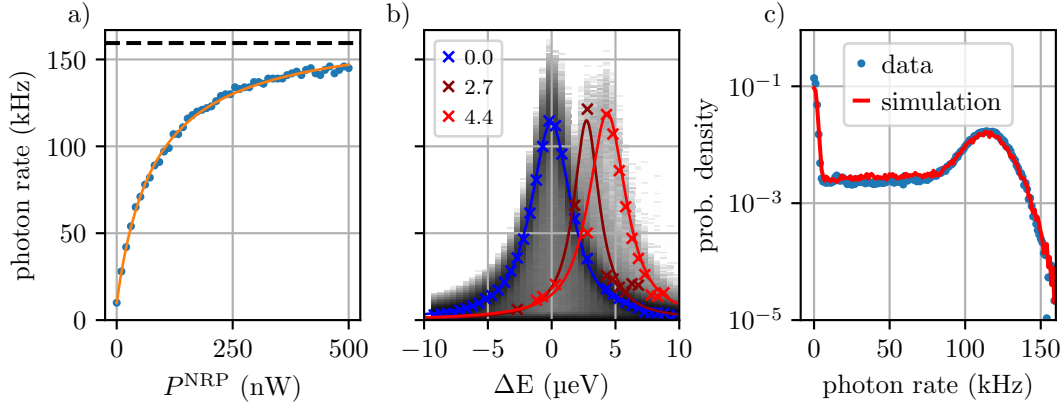


Figure 8. (a) Measured increase of the RF photon rate at X^+ with increasing above band-gap excitation for a constant probe laser intensity of 200 nW (blue dots). The solid orange line depicts a fit according to Eq. 2. (b) Occurrence of an additional resonance at $2.7 \mu\text{eV}$ at finite NRE. (c) Measured relative probabilities of the photon rates (blue dots) and simulation with a straightforward model (red line). The significant “background” level of approximately $2 \cdot 10^{-3}$ is shown in (b) by the greyscale color code, which fills the blue fit and offers insight into the rapid charge dynamics. (b) and (c) are measured at $P^{\text{NRE}} = 222(1) \text{ nW}$ and $V_G = -0.36601(0) \text{ V}$.

Gate voltage dependent RF measurements enabled a detailed study of the QD at various charge states. For negative voltages, the RF shows a weak X^+ transition, with count rates more than an order of magnitude lower than those of the X and X^- transitions. However, the mechanism by which the QD is charged with a hole remains unclear in the case of X^+ . Hole transport from the p-contact to the QD should not be feasible due to the low sample temperature and the built-in, counteracting electric field. Other experiments have observed the X^+ transition before in similar structures [1]. Here, the origin of the QD hole occupation has been assigned inter alia to unintentional C doping in the past [33], which is unavoidable in molecular beam epitaxy. However, according to the band structure, all carbon acceptors in the regime between n-contact and QD should be, in very good approximation, ionized. Creation of holes in the (AlGa)As by below bandgap light due to two-photon absorption or the photo-assisted Shockley-Read-Hall mechanism [34] seems reasonable, but the RF photon rate of the X^+ transition is in our experiment independent of below bandgap optical excitation, ruling out these mechanisms (see Appendix D for details). Quasi-resonant absorption of the RF laser, probing the X^+ transition, could theoretically occur at the nearby X transition—relevant when X^+ lost a hole—if the excited exciton’s electron simultaneously tunnels out of the QD. However, in our experiment, the RF photon rate increases approximately linearly with the probe laser intensity, which does not support this mechanism. Therefore, the specific physical mechanism responsible for loading the QD with a hole remains an open question.

The experiment clearly shows that the X^+ transition can be efficiently recharged through non-resonant optical excitation of the QD quasi-continuum. In this process, the electron from the excited exciton rapidly tunnels out of the QD, leaving a single hole behind. Interestingly, a fast recharging of the QD also increases the dwell time of the hole in the QD, indicating that the hole tunneling out of the QD takes place by tunneling

into ionized acceptor states and not into the (AlGa)As continuum.

Lineshape analyses of the X , X^- , and X^{2-} transitions revealed for our low-noise PIN structure in very good approximation purely Lorentzian lineshapes for the X^- and X^{2-} transitions and a mixture of Lorentzian and Gaussian lineshapes for the X transition. This is interesting in view of transform-limited single-photon sources and, in the case of X^- , concerning potential spin-photon interfaces. However, one has to keep in mind that X^- and X^{2-} are subject to Auger recombination, which has a low yet non-zero probability in GaAs QDs.

V. ACKNOWLEDGMENTS

We thank Ronny Hüther for technical assistance and Nadine Viteritti for the processing of the sample. This work was funded by the Deutsche Forschungsgemeinschaft (DFG, German Research Foundation) under Germany’s Excellence Strategy – EXC-2123 Quantum-Frontiers – 390837967 and OE 177/10-2.

Appendix A: PL Characterization of the QD

Figure 9 shows a PL spectrum of the studied QD for a gate voltage range from -0.75 V to 1 V . The sample temperature is 4 K , the excitation power $20 \mu\text{W}$, the focus diameter $\approx 1 \mu\text{m}$, and the excitation photon energy 1.592 eV . The PL is dispersed by a high-resolution triple spectrometer with an energy resolution of $\approx 20 \mu\text{eV}$ and detected by a liquid nitrogen cooled CCD camera, which covers the PL from 1.559 eV to 1.565 eV . Emission signatures corresponding to exciton complexes ranging from X^{4+} to X^{6-} are observed, with the most prominent transitions occurring for X^+ , X , and X^- . Adjacent charge plateaus exhibit overlap regions where the QD charge state is unstable and switches between two charge states. A comparison of the PL spectra

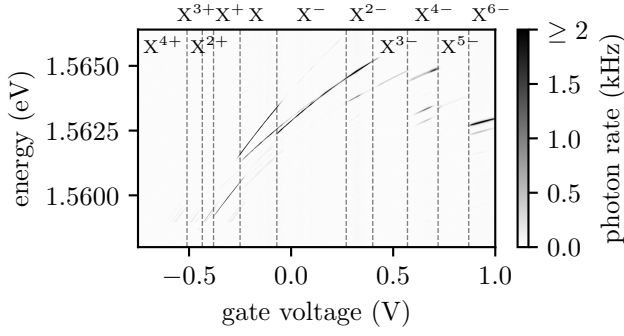


Figure 9. Photoluminescence spectra in dependence on gate voltage in a greyscale colour code.

with the corresponding RF spectra in Fig. 2 reveals a significant Stokes shift for X^{2-} . This occurs because RF probes the $n = 2$ absorption transition, while the PL arises primarily from the $n = 1$ transition due to rapid relaxation of the excited hole to $n = 1$.

Appendix B: Telegraph Data Analysis

In the following, we will first address details concerning the classical switching time analysis of the telegraph signal, which is particularly effective for slow switching times. Subsequently, we will explore the simulation switching time analysis method, which is especially advantageous for fast switching times. In both cases, the continuous stream of photon detection events acquired during the experiment is divided into intervals of binning time t_b , producing telegraph-like signals as shown in Fig. 10(a). Through our evaluation, we determined that for the given QD dynamics, $t_b = 1$ ms provides the optimal balance between time resolution and signal noise.

For slow switching dynamics with timescales significantly exceeding t_b , a switch from one photon rate level to another is clearly resolved by the telegraph signal (as shown in Fig. 10(a)). In this case, the division of the telegraph signal into bright (green) and dim (gray) regions is trivial, and the classical switching time analysis can be applied. To ensure a consistent evaluation, we define a threshold photon rate, as shown in Fig. 10(b), to distinguish between the bright and dim regions. Generally, the bright and dim regions consist of multiple peaks, each representing a QD RF shadow. We consistently set the threshold at the 99% upper confidence interval of the peak with the highest photon emission rate in the dim region. With this approach, the bright and dim time constants τ^{bright} and τ^{dim} can be evaluated using a histogram that is fitted with an exponential decay. Figure 10(c) shows an example of such a fit, which, in this case, yields the characteristic switching time of the bright state 0, denoted by τ_0^{bright} .

In the case of rapid switching dynamics on the timescale of t_b , the telegraph signal cannot adequately resolve individual switching events and a meaningful division into bright and dim intervals becomes impossible. In fact, the probability density of such a telegraph signal is characterized by a prominent high background, as

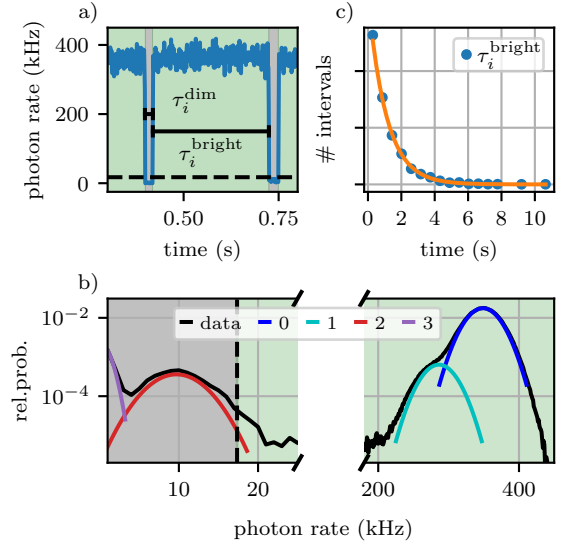


Figure 10. (a) Snippet of a telegraph signal showing two switching events. The threshold (black dashed line) divides the signal into bright and dim intervals with switching times τ_i^{bright} and τ_i^{dim} . (b) Exemplary probability density of X^- including all visible shadow resonances, each fitted by a Gaussian. Again, the threshold (black dashed line) separates the probability density into a bright and dim region. (c) Histogram of τ_i^{bright} and a fit by an exponential decay (orange curve) revealing the characteristic switching time τ_i^{bright} .

shown in Fig. 8(c), which originates from not properly resolved switching events. Since this dynamics cannot be evaluated by the classical switching time analysis, a simulation switching time analysis is employed instead. In this scenario, an artificial photon stream is simulated, taking into account two or more photon emission levels of the QD and additionally the switching dynamics between these levels. The probability density calculated in this way is then compared with the experiment, and the parameters of the simulation are adjusted until the simulation and experiment match perfectly. Figure 8(c) illustrates such a simulation considering the simplest case of two emission levels, which are located at 115 kHz and 0 kHz. For the data shown, the analysis indicates a switching time of 2 ms between the two levels.

1. Non resonant excitation case for X^+

Following the classical switching time analysis outlined above, Fig. 11(a) presents for X^+ the probability density for nonresonant excitation at a P^{NRE} of 222 nW and a detuning of $\Delta E = 0.3 \mu\text{eV}$. At this detuning, not all shadow resonances of the X^+ transition, which are visible in Fig. 8(b), can be clearly resolved, allowing only for three peaks to be unambiguously fitted by three Gaussian functions. A phenomenological background accounts for the constant offset between the peaks. The threshold (indicated by the black dashed line) once again divides the probability density into a bright and a dim region.

Figure 11(b) shows the extracted switching rates corresponding to these bright and dim intervals. Both

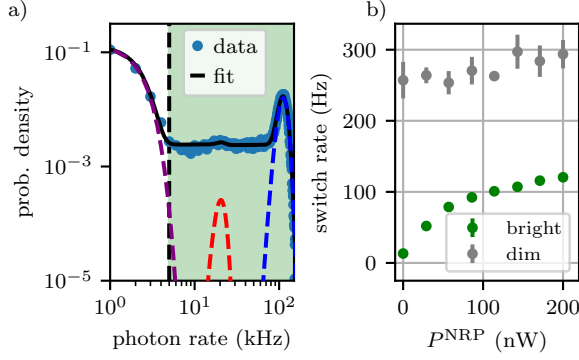


Figure 11. (a) Probability density of X^+ measured at $P^{\text{NRE}} = 222 \text{ nW}$ and a detuning of $\Delta E = 0.3 \mu\text{eV}$. The probability density is fitted by three Gaussian functions along with a constant background between the peaks induced by NRE. The threshold (vertical dashed line) divides the probability density into a dim (grey) and a bright (green) region. (b) Switching rates $\gamma^{\text{dim}} = 1/\tau^{\text{dim}}$ and $\gamma^{\text{bright}} = 1/\tau^{\text{bright}}$ in dependence of P^{NRE} .

rates increase with NRE power, although the bright-state rate remains consistently lower than the dim-state rate, indicating that the QD tends to spend more time in the bright state. This trend is further corroborated by results from the simulation-based switching-time analysis (data not shown). Similar measurements at the X and X^- transition (data not shown) show a similar trend.

Appendix C: Spin Noise Measurement

Spin noise spectroscopy (SNS) is a versatile tool to investigate the spin and charge dynamics in semiconductors, down to the level of a single QD [12, 16, 35, 36]. Spin and charge fluctuations are imprinted onto the linear polarization axis of the probe beam and are measured using a polarization bridge and a balanced photo detector [37, 38]. The detector used in this work features a bandwidth of 220 kHz, which increases the time resolution of the experiments from the millisecond to the microsecond regime, compared to the RF measurements. The probe laser intensity was increased to $2 \mu\text{W}$ for the SNS measurements to counter the reduced signal-to-noise ratio compared to the RF measurements, which utilize single photon avalanche photo diodes.

Figure 12 displays a representative spin noise (SN) spectrum near the QD resonance, revealing two components, each described by a Lorentzian contribution: a slow component (L1) in the kilohertz range, attributed to the charge dynamics of the Si donors, and a fast component (L2) in the 100 kHz range, associated with the tunneling dynamics of the resident hole in the QD for the X^+ state. We want to emphasize that this assignment was only possible with the combined insights gained by the RF and SNS measurements.

Introducing a second non-resonant laser results in an increase in the rates of both components, as illustrated in Fig. 13. Notably, the noise power associated with L1 rises significantly, marking an overall increase of Si donor related switching events, which is consistent with

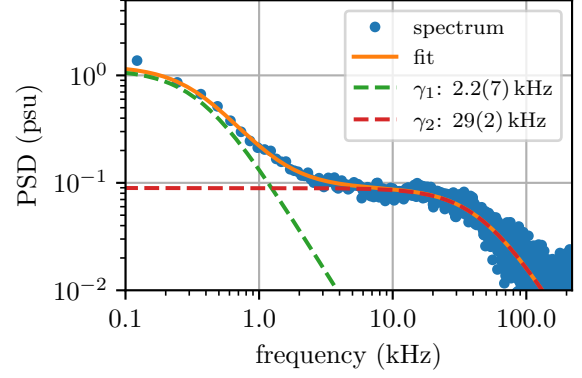


Figure 12. Typical SN spectrum for a quasi-resonant probe laser with a detuning of $0.64 \mu\text{eV}$ and an intensity of $2 \mu\text{W}$. The power spectral density (PSD) is plotted in power spectral units (psu). The combination of two Lorentzian contributions describes the spectrum in excellent agreement. The first component (green) is identified with the Si donor charge dynamics, while the second contribution (red) is identified with the fast hole occupancy dynamics of the QD.

the observations in the RF measurements. In contrast, the amplitude of L2 decreases, suggesting a reduction in the number of hole tunneling events. Interestingly, despite the reduced amplitude, the rate associated with L2 increases. This apparent contradiction can be explained by an enhanced hole tunneling rate into the QD, accompanied by an increased residence time of the hole within the dot. We attribute this behavior to carbon

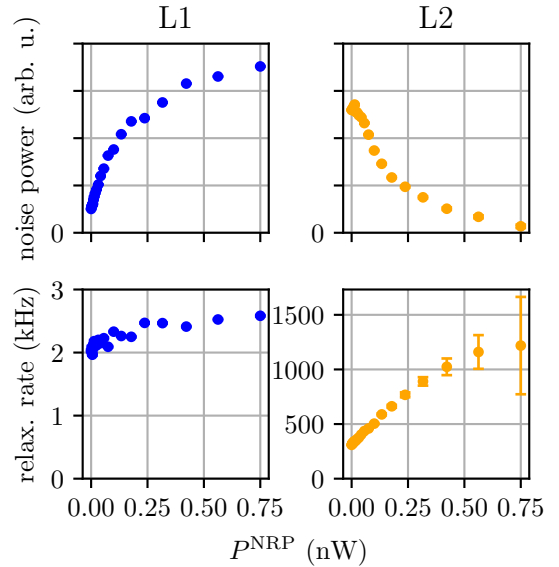


Figure 13. Parameters of the slow (L1) and fast (L2) Lorentzian components of individual spin noise spectra as a function of P^{NRE} . The noise amplitude of L1 increases significantly with P^{NRE} , indicating a higher number of switching events associated with Si donors. This is accompanied by an increase in the corresponding relaxation rate. In contrast, the noise power of L2 decreases markedly, suggesting a reduction in hole recharging events, while its relaxation rate also increases. Together, these trends suggest a scenario of faster hole charging accompanied by an increased dwell time of the hole in the QD.

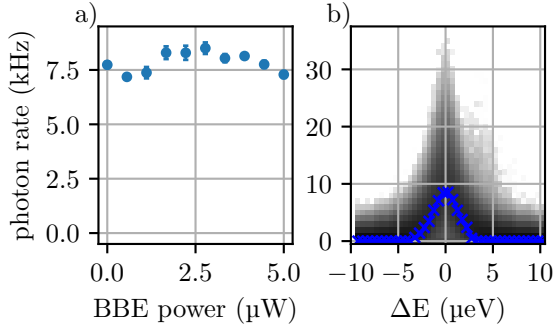


Figure 14. (a) Most probable RF photon rate at the center of the dominant X^+ transition versus below bandgap excitation power. (b) Greyscale color plot of the photon rate probability in dependence on detuning. The blue solid line depicts a pseudo-Voigt fit, as in Fig. 4.

impurities in the vicinity of the QD becoming saturated with holes due to the non-resonant excitation.

Appendix D: Below Bandgap Excitation

Figure 14 depicts the most probable RF photon rate of the dominant X^+ transition in dependence on below bandgap excitation (BBE) with a laser photon energy of 1.53 eV. The laser photon energy is well below the X^+ QD transition and the (AlGa)As bandgaps, effectively excluding the possibility of band-to-band single photon excitation by BBE. In principle, two-photon absorption processes might be feasible and create holes in or close to the QD. However, despite the BBE power reaching up to 5 μW, the measured RF photon rate remains constant, indicating that BBE does not have a measurable impact on the charging of the X^+ transition.

- [1] L. Zhai, M. C. Löbl, G. N. Nguyen, J. Ritzmann, A. Javadi, C. Spinnler, A. D. Wieck, A. Ludwig, and R. J. Warburton, *Nature Communications* **11**, 4745 (2020).
- [2] J. Neuwirth, F. Basso Basset, M. B. Rota, E. Roccia, C. Schimpf, K. D. Jöns, A. Rastelli, and R. Trotta, *Materials for Quantum Technology* **1**, 043001 (2021).
- [3] Y. Arakawa and M. J. Holmes, *Applied Physics Reviews* **7**, 021309 (2020).
- [4] J. Houel, A. Kuhlmann, L. Greuter, F. Xue, M. Poggio, B. D. Gerardot, P. A. Dalgarno, A. Badolato, P. M. Petroff, A. Ludwig, D. Reuter, A. D. Wieckand, and R. J. Warburton, *Physical Review Letters* **108**, 107401 (2012).
- [5] A. V. Kuhlmann, J. Houel, A. Ludwig, L. Greuter, D. Reuter, A. D. Wieck, M. Poggio, and R. J. Warburton, *Nature Physics* **9**, 570 (2013).
- [6] M. Hauck, F. Seilmeier, S. E. Beavan, A. Badolato, P. M. Petroff, and A. Högele, *Physical Review B* **90**, 235306 (2014).
- [7] J. Hansom, C. H. H. Schulte, C. Matthiesen, M. J. Stanley, and M. Atatüre, *Applied Physics Letters* **105**, 172107 (2014).
- [8] N. Ha, T. Mano, Y.-L. Chou, Y.-N. Wu, S.-J. Cheng, J. Bocquel, P. M. Koenraad, A. Ohtake, Y. Sakuma, K. Sakoda, and T. Kuroda, *Physical Review B* **92**, 075306 (2015).
- [9] A. Al-Ashouri, A. Kurzmann, B. Merkel, A. Ludwig, A. D. Wieck, A. Lorke, and M. Geller, *Nano Letters* **19**, 135 (2019).
- [10] J. Kerski, P. Lochner, A. Ludwig, A. Wieck, A. Kurzmann, A. Lorke, and M. Geller, *Physical Review Applied* **15**, 024029 (2021).
- [11] A. Kurzmann, A. Ludwig, A. D. Wieck, A. Lorke, and M. Geller, *Nano Letters* **16**, 3367 (2016).
- [12] J. Wiegand, D. S. Smirnov, J. Osberghaus, L. Abaspour, J. Hübner, and M. Oestreich, *Physical Review B* **98**, 125426 (2018).
- [13] A. Kurzmann, P. Stegmann, J. Kerski, R. Schott, A. Ludwig, A. D. Wieck, J. König, A. Lorke, and M. Geller, *Physical Review Letters* **122**, 247403 (2019).
- [14] P. Lochner, A. Kurzmann, J. Kerski, P. Stegmann, J. König, A. D. Wieck, A. Ludwig, A. Lorke, and M. Geller, *Nano Letters* **20**, 1631 (2020).
- [15] P. Lochner, J. Kerski, A. Kurzmann, A. D. Wieck, A. Ludwig, M. Geller, and A. Lorke, *Physical Review B* **103**, 075426 (2021).
- [16] P. Sterin, K. Hühn, M. M. Glazov, J. Hübner, and M. Oestreich, *Physical Review B* **108**, 125301 (2023).
- [17] H. G. Babin, J. Ritzmann, N. Bart, M. Schmidt, T. Kruck, L. Zhai, M. C. Löbl, G. N. Nguyen, C. Spinnler, L. Ranasinghe, R. J. Warburton, C. Heyn, A. D. Wieck, and A. Ludwig, *Nanomaterials* **11**, 2703 (2021).
- [18] S. F. C. da Silva, G. Undeutsch, B. Lehner, S. Manna, T. M. Krieger, M. Reindl, C. Schimpf, R. Trotta, and A. Rastelli, *Applied Physics Letters* **119**, 120502 (2021).
- [19] A. V. Kuhlmann, J. Houel, D. Brunner, A. Ludwig, D. Reuter, A. D. Wieck, and R. J. Warburton, *Review of Scientific Instruments* **84**, 073905 (2013).
- [20] We observed that the polarization extinction exhibits a significant wavelength dependence, making the additional color filter essential for the far-detuned non-resonant laser.
- [21] Excelitas SPCM-AQRH-15-FC, saturation rate: 37 MHz.
- [22] Alazartech ATS9360, operated at a sampling rate of 180 MHz.
- [23] Attocube ANSxyz100std/LT, ANPx102/RES/LT/HV and ANPz102/RES/LT/HV.
- [24] X. Xu, A. Andreev, and D. A. Williams, *New Journal of Physics* **10**, 053036 (2008).
- [25] P. W. Fry, I. E. Itskevich, D. J. Mowbray, M. S. Skolnick, J. J. Finley, J. A. Barker, E. P. O'Reilly, L. R. Wilson, I. A. Larkin, P. A. Maksym, M. Hopkinson, M. Al-Khafaji, J. P. R. David, A. G. Cullis, G. Hill, and J. C. Clark, *Physical Review Letters* **84**, 733 (2000).
- [26] Strictly speaking, these values contain a very small systematic error, as both photon leakage and dark counts ($\lesssim 1$ kHz) are always present.
- [27] J. D. Mar, X. L. Xu, J. J. Baumberg, F. S. F. Brossard, A. C. Irvine, C. Stanley, and D. A. Williams, *Physical Review B* **83**, 075306 (2011), publisher: American Physical Society.
- [28] The neighboring QDs have a significantly larger transition energy, which probably inhibits charge changes at moderate V_G .
- [29] B. Chen, Q.-M. Zhang, and J. Bernholc, *Physical Review B* **49**, 2985 (1994).
- [30] K. J. Beernink, R. L. Thornton, G. B. Anderson, and M. A. Emanuel, *Applied Physics Letters* **66**, 2522 (1995).

- [31] P. M. Mooney, *Journal of Applied Physics* **67**, R1 (1990).
- [32] E. Muñoz, E. Calleja, I. Izpura, F. García, A. L. Romero, J. L. Sánchez-Rojas, A. L. Powell, and J. Castagné, *Journal of Applied Physics* **73**, 4988 (1993).
- [33] M. Hayne, O. Razinkova, S. Bersier, R. Heitz, L. Müller-Kirsch, M. Geller, D. Bimberg, and V. V. Moshchalkov, *Physical Review B* **70**, 081302 (2004), publisher: American Physical Society.
- [34] B. Vest, B. Fix, J. Jaeck, and R. Haïdar, *Journal of the European Optical Society-Rapid Publications* **12**, 26 (2016).
- [35] R. Dahbashi, J. Hübner, F. Berski, K. Pierz, and M. Oestreich, *Physical Review Letters* **112**, 156601 (2014).
- [36] J. Wiegand, D. S. Smirnov, J. Hübner, M. M. Glazov, and M. Oestreich, *Physical Review B* **97**, 081403 (2018).
- [37] J. Hübner, F. Berski, R. Dahbashi, and M. Oestreich, *physica status solidi (b)* **251**, 1824 (2014).
- [38] M. M. Glazov and V. S. Zapasskii, *Optics Express* **23**, 11713 (2015).